Solid State Sciences 169 (2025) 108060

Contents lists available at ScienceDirect

Solid State Sciences

journal homepage: www.elsevier.com/locate/ssscie

P-type thermoelectric properties of $TiNi_{1-x-y}Co_ySn$ half-Heusler alloy with reduced interstitial Ni atoms

Kosuke Yamazaki [a], Sopheap Sam [b,c], Hiroshi Nakatsugawa [a,*]

[a] Yokohama National University, Graduate School of Engineering Science, 79-5 Tokiwadai, Hodogaya, Yokohama, 240-8501, Kanagawa, Japan
[b] Institute of Technology of Cambodia, Faculty of Electrical Engineering, Department of Industrial and Mechanical Engineering, Russian Federation Blvd, P.O. Box 86, Phnom Penh, 120404, Cambodia
[c] Institute of Technology of Cambodia, Research and Innovation Center, Russian Federation Blvd, P.O. Box 86, Phnom Penh, 120404, Cambodia

ARTICLE INFO

Keywords:
Thermoelectrics
Seebeck effect
Half-Heusler
TiNiSn
Interstitial Ni atoms

ABSTRACT

TiNiSn is an N-type thermoelectric material with low toxicity. The electrical conduction of TiNiSn can be tuned from N-type to P-type by substituting Co atoms at Ni sites. However, the *ZT* value is lower than that of the N-type TiNiSn, primarily due to its higher electrical resistivity. To decrease the electrical resistivity, it is necessary to increase the carrier density or mobility; however, the absolute value of the Seebeck coefficient decreases, which has a trade-off relationship with the electrical resistivity. To solve this problem, we prepared P-type thermoelectric materials $TiNi_{1-x-y}Co_ySn$ ($0 \le x \le 0.1$, $0.01 \le y \le 0.05$) with reduced interstitial Ni atoms by arc melting and heat treatment process. As a result, we successfully improved the electrical conductivity while maintaining the Seebeck coefficient. The hole carrier density increases as the number of interstitial Ni atoms decreases, and the electrical resistivity decreases by 78 % from 2.78×10^{-2} Ωcm (for $x = 0$, $y = 0.05$) to 6.02×10^{-3} Ωcm (for $x = 0.03$, $y = 0.05$) at 300 K. The *ZT* value increases by a factor of 1.5 ($ZT_{max} = 0.18$ at 700 K) for $TiNi_{0.92}Co_{0.05}Sn$ compared to $TiNi_{0.95}Co_{0.05}Sn$, indicating that the reduction of interstitial Ni atoms is effective in improving the thermoelectric properties of the P-type half-Heusler alloy TiNiSn. The peak *ZT* of 0.18 remains below the level required for practical implementation; however, this can be further improved by decreasing the lattice thermal conductivity.

1. Introduction

Thermoelectric (TE) technology enables the direct conversion of waste heat into electrical energy, offering significant potential for realizing an energy-efficient society [1,2]. A thermoelectric generator (TEG) is a type of environmental power generation that can be used to recover waste heat to power IoT devices. However, due to the low conversion efficiency, the application of TEG devices is still limited [3]. For the practical implementation of TEG, it is necessary to achieve high conversion efficiency. In order to improve the thermoelectric conversion efficiency, we need to utilize high-performance materials. The performance of TE materials is characterized by:

$$ZT = \frac{S^2}{\rho \cdot (\kappa_{ele} + \kappa_{lat})} T \quad (1)$$

where *ZT* is the dimensionless figure of merit, *S* is the Seebeck coefficient, *T* is temperature, ρ is electrical resistivity, and κ is thermal conductivity, where κ consists of carrier thermal conductivity κ_{ele} and lattice thermal conductivity κ_{lat} ($\kappa = \kappa_{ele} + \kappa_{lat}$). $S^2\rho^{-1}$ is called the power factor (PF). Therefore, *ZT* can be improved by increasing PF and decreasing κ.

Generally, a TE module consists of P-type and N-type elements [4,5]. Therefore, improving *ZT* values for both P-type and N-type significantly contributes to enhancing the device efficiency. In recent years, the search for thermoelectric materials with high thermal stability and durability has been conducted to reach practical application [6,7]. Those materials may include oxide [8,9], silicide [10,11], and Heusler [12–16]. A good thermoelectric material should exhibit good thermal stability while operating at high temperatures. To achieve this goal, we focus on the half-Heusler (HH) alloy TiNiSn, which is one of the practical thermoelectric materials due to its relatively low cost, low toxicity, and chemical stability at high temperatures (<1273 K) [17,18].

This article is part of a special issue entitled: Thermoelectric & Topology published in Solid State Sciences.

* Corresponding author.
E-mail address: nakatsugawa-hiroshi-dx@ynu.ac.jp (H. Nakatsugawa).

https://doi.org/10.1016/j.solidstatesciences.2025.108060
Received 2 July 2025; Received in revised form 23 August 2025; Accepted 1 September 2025
Available online 5 September 2025

The crystal structure of TiNiSn is MgAgAs type (Space Group F–43m, No. 216), where Ti and Sn form a rock salt structure (NaCl) and Ni atoms occupy half of the sublattice. Half of the sublattice is vacancies, TiNiSn, showing a high power factor [19], but exhibits a high lattice thermal conductivity (κ_{lat}) due to its simple crystal structure. Therefore, many studies have been conducted to increase ZT by decreasing κ_{lat}. For example, as reported in Refs. [20,21], the κ_{lat} was decreased by increasing phonon scattering through nanostructures, fine precipitates, and microstructure control. The results of a reduction in thermal conductivity from 3.9 to 4.4 $Wm^{-1}K^{-1}$ (T = 323 K–823 K) to 2.3 $Wm^{-1}K^{-1}$ (T = 523 K) have also been reported [22]. Although the sample prepared by powder metallurgy technique yields a low κ_{lat} value, it usually has the disadvantage of increasing ρ due to the formation of oxidation impurities [23]. The conduction properties of TiNiSn can be controlled by changing the majority of charge carriers [21,24,25]. We have recently succeeded in making P-type TiNiSn by Co substitution at the Ni site, and found that the largest ZT for P-type thermoelectric material $TiNi_{1-y}Co_ySn$ ($0 \le y \le 0.15$) is $ZT = 0.12$ (T = 675 K) when $y = 0.05$ [26], but this value is less than half that of N-type TiNiSn [27–29]. The main reason for the low ZT is the high ρ. According to previous studies on intrinsic defects in the TiNiSn system, TiNiSn was reported to form interstitial Ni atoms in which Ni atoms occupy the 4d sites, which should be vacancies in the stoichiometric composition [30–33]. This intrinsic defect (interstitial Ni atoms) is the lowest formation energy among several other defects formed in TiNiSn and is therefore more easily formed than any other intrinsic defects. Some previous studies using first-principles calculations have reported that interstitial Ni atoms are defects that are easily formed[33–35]. The same tendency is also observed in the similar HH compound MNiSn (M = Ti, Zr, Hf) [15,36]. The interstitial Ni atoms are considered to act as donor impurities to the system, and in the P-type, they promote the increase of electrical resistivity due to the electroneutrality condition. In addition, according to Sun et al. [36], the removal of interstitial Ni atoms by decreasing the Ni composition ratio improves the mobility, which affects the relaxation time of the carrier.

As mentioned above, it is considered that the removal of interstitial Ni atoms in the P-type thermoelectric material $TiNi_{1-y}Co_ySn$ could effectively decrease ρ by increasing the hole carrier density and mobility. However, the increase in carrier density and mobility generally decreases the absolute value of the Seebeck coefficient [37], but this is not the case when the electronic states change. Ai et al. reported that E_g changes in HfNiSn when the interstitial Ni atoms are reduced [15]. Since the expansion of E_g contributes to the enhancement of $|S|$, the removal of interstitial Ni atoms is expected to have a positive effect on $|S|$. However, to our knowledge, the comprehensive investigation of P-type TiNiSn compounds with reduced interstitial Ni atoms, including the ZT values, has not been reported.

Therefore, we prepared $TiNi_{1-x-y}Co_ySn$ ($0 \le x \le 0.1$, $0 \le y \le 0.05$) by the arc melting method, which is free from oxide impurities and produced high-density samples, and measured thermoelectric properties up to 800 K to obtain maximum ZT values. This study aims to improve the ZT of Co-substituted TiNiSn compounds by reducing the interstitial Ni atoms and optimizing the thermoelectric properties.

2. Experimental method

2.1. Sample preparation

The raw elements of Ti (grain, 99.9 % up), Ni (grain, 99 %), Co (powder, 99 % up), and Sn (grain, 99.9 % up) were weighed to follow the composition ratio of $TiNi_{1-x-y}Co_ySn$ (x = 0, 0.01, 0.03, 0.05, 0.08, 0.1, y = 0.01, 0.03, 0.05), and the total weight is 15 g. From our recent report [26], since it is clear that ZT decreases with $y > 0.05$, the composition is limited to $y = 0.05$. Since the Co substitution level greatly affects the carrier density, we also fabricated y = 0.01 and 0.03 were prepared. (This paper describes only the results for y = 0.05, which showed good thermoelectric properties. The results for y = 0.01 and 0.03 are described in the supplementary information(SI).) The weighed materials were melted in an arc melting furnace with high-purity Ar gas introduced at 5 kPa. Ti was first melted as an oxygen getter to react with any residual air in the chamber. In this process, the ingots were flipped and remelted several times on each side. The arc power gradually increased because if we increase the power too fast, it may cause the material to fly out of the copper heart's mold. The distance between the electrode and the sample was carefully maintained to prevent direct contact. After arc-melting, the samples were cut into measurable dimensions by a wire electric discharge machine (EC-3025, Makino). The cut samples were vacuum-sealed to prevent oxidation and homogenized at 1073 K for 168 h. We confirm the heat treatment conditions using ternary TiNiSn. In Supporting Information (SI), Fig. S1 shows the XRD patterns before and after heat treatment for TiNiSn. Although there were many unreacted phases before the heat treatment, the heat treatment resulted in the formation of almost a single phase. Fig. S2 shows SEM-EDS mapping images of the samples used for measurements of ρ, S, and κ. From the elemental distribution analysis, it is confirmed that the samples obtained by the arc melting method were homogenized.

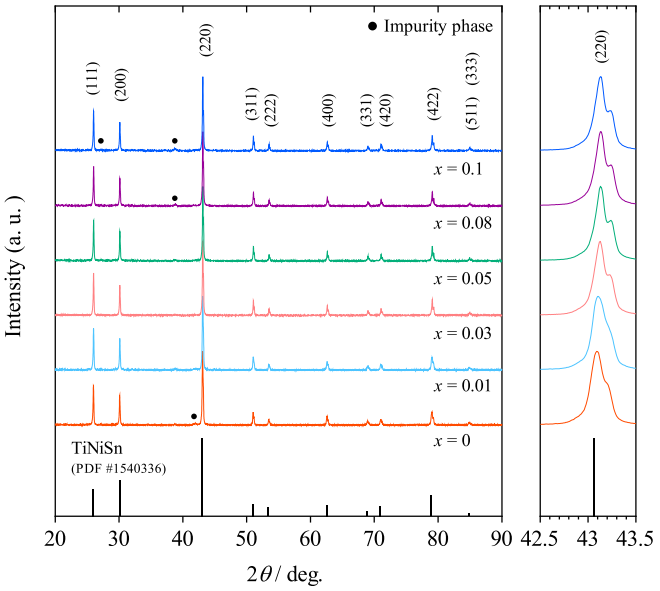

Fig. 1. XRD profiles of $TiNi_{0.95-x}Co_{0.05}Sn$ ($0 \le x \le 0.1$, y = 0.05) at room temperature, where the indexed peaks represent the half-Heusler phase.

2.2. Characterization method

Powder X-ray diffraction measurements (SmartLab, Rigaku, Cu Kα: λ = 1.5418 Å) were performed to investigate the crystal structure of the samples, and the obtained X-ray diffraction profiles were used to identify the crystal structure by Rietveld refinement in the RIETAN-FP program [38]. The density of samples was measured by the Archimedes method. It was confirmed that high-density samples of 6.9–7.1 gcm^{-3} (>95 % relative density) were obtained for all samples. ICP-OES (ICPE-9000, SHIMADZU) was used for compositional analysis. Elemental distribution on the sample surface was observed using SEM-EDS (SU8010, HITACHI High-Tech). Sample surfaces are polished using EcoMet250 + AutoMet250 (BUEHLER). To determine the carrier density and mobility, the Hall coefficient was measured at room temperature using Hall measurement equipment (ResiTest8300, TOYO Co.). Electrical resistivity and Seebeck coefficient were measured at temperatures ranging from 80 K to 395 K using ResiTest8300 and from 395 K to 800 K using a home-built apparatus. Thermal conductivity was measured in the range of 300 K–800 K using a power efficiency

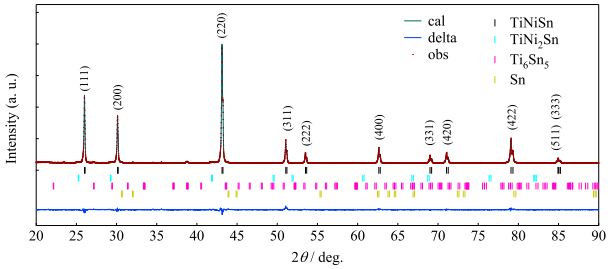

Fig. 2. Rietveld refinement of $TiNi_{0.95-x}$ $Co_{0.05}Sn$ ($x = 0.03$, $y = 0.05$) at diffraction angles of $20° \leq 2\theta \leq 90°$, where the indexed peaks represent the half-Heusler phase.

measurement system (PEM-2, ULVAC, Inc.). The κ of a sample is obtained from the following equation.

$$\kappa = \frac{WA}{\Delta T}\cdot\frac{t}{ab} \tag{2}$$

where W is the heat flow density that penetrates the copper block, A is the cross-sectional area of the copper block, ΔT is the temperature difference of the sample, and a, b, and t are the sample lengths, width, and thickness, respectively.

3. Results and discussion

3.1. Structure and compositional analysis

Fig. 1 shows the result of powder X-ray diffraction measurements for $TiNi_{1-x-y}Co_ySn$ ($0 \leq x \leq 0.1$, $y = 0.05$). The results of $TiNi_{1-x-y}Co_ySn$ ($0 \leq x \leq 0.1$, $y = 0.01$, 0.03) are also shown in Fig. S3 of the Supporting Information (SI). The indexed peaks in the figure are the peaks of the HH structure. This indicates that the samples were mainly crystallized in the HH phase with a trace of an impurity phase. The trace of impurity phase is due to the formation of TiNiSn by the peritectic reaction [39]. However, the peak intensity of the impurity phase is very small compared to the main HH phase, suggesting that all samples are mainly grown in the HH phase. For $x = 0.03$, $y = 0.05$, the X-ray diffraction profile after Rietveld analysis is shown in Fig. 2. The crystallographic parameters after the analysis are summarized in Table 1. The reliability factor R_{wp} is less than 10 % for all the samples, and a good refinement of the crystallographic parameters is obtained. The x dependence of the lattice parameter after Rietveld analysis is shown in Fig. 3 (a). The lattice parameter is constant for $x \geq 0.02$. Fig. 3 (b) shows the x dependence of phase fractions. All of the prepared samples are mostly occupied by the main phase, but a decrease in the main phase is observed for $x > 0.05$. The increase in the Ti_6Sn_5 phase coincides with the decrease in the main phase, suggesting that an excessive decrease in the Ni composition ratio leads to the formation of Ti_6Sn_5, which deteriorates thermoelectric properties. The increase in impurity phase with increasing x shows a similar trend for $y = 0.01$, 0.03 (Table ST1 in the SI). The phase fractions of $TiNi_2Sn$ and Sn are constant regardless of the decrease in the Ni

Table 1
Crystal structure parameters for $TiNi_{0.95-x}Co_{0.05}Sn$ ($0 \leq x \leq 0.1$, $y = 0.05$) at room temperature refined by the Rietveld analysis.

Samples		$TiNi_{0.95-x}Co_{0.05}Sn$					
Space group		*F*–43*m*					
Composition, x		0	0.01	0.03	0.05	0.08	0.1
Composition, y		0.05					
$a = b = c$ (Å)		5.93219 (4)	5.93105 (4)	5.92764 (4)	5.92704 (4)	5.9269 (4)	5.92723 (4)
V (Å^3)		208.759 (3)	208.638 (3)	208.279 (3)	208.216 (2)	208.201 (2)	208.236 (3)
Ti	x	0	0	0	0	0	0
	y	0	0	0	0	0	0
	z	0	0	0	0	0	0
	B (Å^2)	0.50	0.50	0.50	0.50	0.50	0.50
	g	1.0	1.0	1.0	1.0	1.0	1.0
Ni1	x	0.25	0.25	0.25	0.25	0.25	0.25
	y	0.25	0.25	0.25	0.25	0.25	0.25
	z	0.25	0.25	0.25	0.25	0.25	0.25
	B (Å^2)	0.50	0.50	0.50	0.50	0.50	0.50
	g	0.912 (2)	0.897 (2)	0.922 (2)	0.917 (2)	0.922 (2)	0.920 (2)
Co	x	0.25	0.25	0.25	0.25	0.25	0.25
	y	0.25	0.25	0.25	0.25	0.25	0.25
	z	0.25	0.25	0.25	0.25	0.25	0.25
	B (Å^2)	0.50	0.50	0.50	0.50	0.50	0.50
	g	0.05	0.05	0.05	0.05	0.05	0.05
Ni2	x	0.75	0.75	0.75	0.75	0.75	0.75
	y	0.75	0.75	0.75	0.75	0.75	0.75
	z	0.75	0.75	0.75	0.75	0.75	0.75
	B (Å^2)	0.50	0.50	0.50	0.50	0.50	0.50
	g	0.072 (2)	0.060 (2)	0.007 (2)	0.018 (2)	0.047 (2)	0.028 (2)
Sn	x	0.50	0.50	0.50	0.50	0.50	0.50
	y	0.50	0.50	0.50	0.50	0.50	0.50
	z	0.50	0.50	0.50	0.50	0.50	0.50
	B (Å^2)	0.50	0.50	0.50	0.50	0.50	0.50
	g	1.0	1.0	1.0	1.0	1.0	1.0
R_{wp} (%)		2.504	2.487	2.570	2.485	2.417	2.622
R_P (%)		1.751	1.768	1.798	1.734	1.721	1.823
R_e (%)		1.365	1.365	1.371	1.322	1.313	1.395
S (= R_{wp}/R_e)		1.834	1.822	1.874	1.880	1.840	1.880
R_B (%)		2.945	2.774	3.773	2.615	2.313	3.329
R_F (%)		1.559	1.460	1.943	1.199	1.218	1.541
Mass fractions (%)	TiNiSn	95.12	94.28	94.75	94.53	93.63	92.19
	$TiNi_2Sn$	2.09	1.60	1.16	1.31	1.18	1.21
	Ti_6Sn_5	1.30	2.78	2.42	2.62	3.77	5.19
	Sn	1.49	1.34	1.67	1.54	1.42	1.41

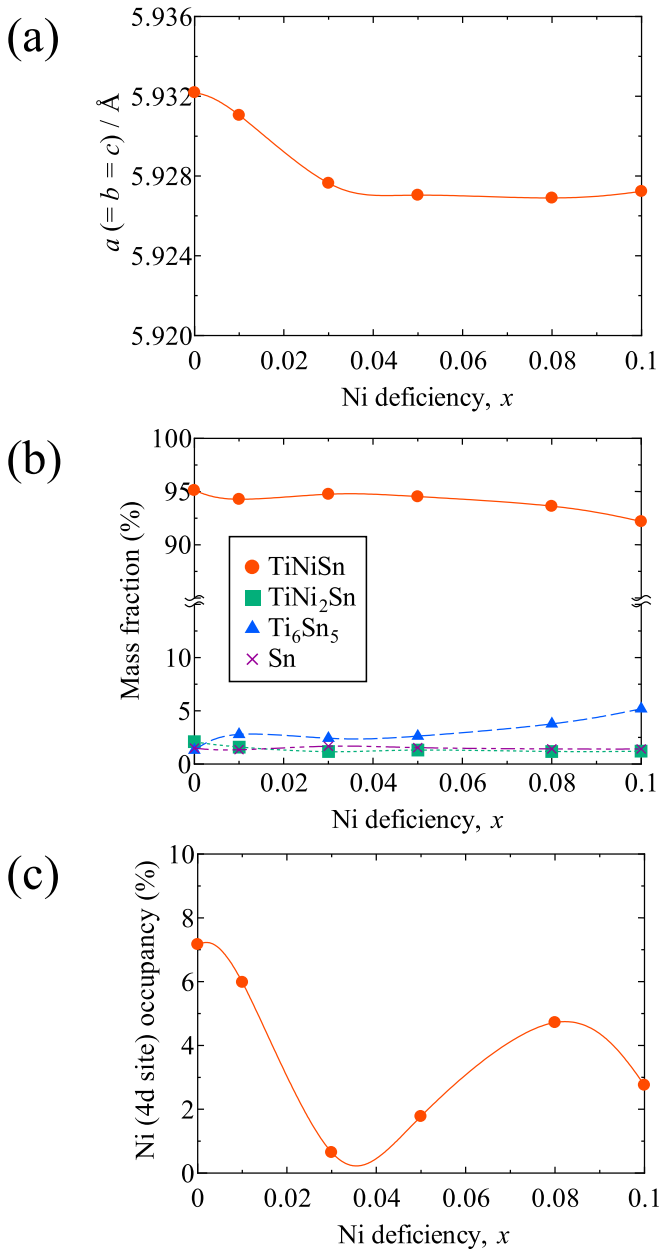

Fig. 3. (a) Lattice constants (b) Mass fractions (c) Ni defect of $TiNi_{0.95-x}Co_{0.05}Sn$ ($0 \leq x \leq 0.1$, $y = 0.05$) depending on Ni deficiency.

composition ratio. Fig. 3 (c) shows the occupancy of Ni atoms at 4d sites, which are considered as interstitial Ni atoms. The decrease in the occupancy for $x > 0$ suggests that the interstitial Ni atoms are suppressed by the decrease in the Ni composition ratio. In particular, for $x = 0.03$ and $y = 0.05$, the occupancy shows a minimum. For $x > 0.05$, the 4d sites occupancy again turns to increase, and this result is similar to the experimental results obtained by decreasing the Ni composition ratio in the HH alloy HfNiSn, which has the same crystal structure [15]. This is thought to be due to the mechanism of phase formation. TiNiSn is formed by peritectic reaction [39]. This occurs when the higher melting point $TiNi_2Sn$ phase and Ti_6Sn_5 phase precipitate first, and the TiNiSn phase is formed around them. When the decrease in Ni composition ratio is small, the effect on the formation of the main phase is minimal, and since the total number of Ni atoms decreases, the number of excess Ni atoms also decreases, resulting in a reduction in interstitial Ni atoms. However, a decrease of $x = 0.05$ or more causes a significant imbalance in the composition ratio, leading to an increase in the amount of the impurity phase Ti_6Sn_5. As a result, a large amount of Ti and Sn is consumed, leading to an excess of Ni in the surrounding area, which in turn causes interstitial Ni atoms to form again. In fact, Table 1, which is the Rietveld analysis results, clearly shows a tendency for impurity phases to increase as the Ni composition ratio decreases. Therefore, it is considered that this is a common trend in MNiSn (M = Ti, Zr, and Hf), and that an excessive decrease in the Ni composition ratio increases interstitial Ni atoms, while a small amount of decrease is effective in suppressing interstitial Ni atoms. In addition, this result indicates that it is possible to reduce interstitial Ni atoms even in samples fabricated solely by arc melting and heat treatment. Therefore, it is possible to optimize interstitial Ni atoms by changing the composition ratio, even with different fabrication methods. However, the high-temperature melting process alone leaves a large amount of unreacted phase remaining. In this case, prolonged heat treatment is necessary. There is no systematic change between the interstitial Ni atoms and Ni deficiency for $y = 0.01$ and 0.03 (Table ST1 in the SI). It suggests that the different amount of Co substitution affects the formation of interstitial Ni atoms.

Table 2 shows compositional analysis using ICP-OES. All the samples show values close to the nominal compositions, with Ni decreasing as x increases. The results of $y = 0.01$, 0.03 are also the same (Table ST2 in the SI). The slightly lower values of Sn compared to Ti and Ni are probably due to its lower melting point compared to other elements, which may have been reduced during the fabrication process. The decrease in Sn was also observed in other fabrication methods [22,40,41] and is considered to be a phenomenon unique to compounds with significantly different melting points. In order to solve this problem, we used the method of doping excessively with Sn. When TiNiSn with excessively added Sn was fabricated by the same method, the impurity phase of Sn increased. Since the increase in the impurity phase is expected to deteriorate the thermoelectric properties, the raw materials were weighed based on their stoichiometric compositions in this study. Fig. 4 shows the SEM image and elemental distribution for $x = 0.1$, $y = 0.05$. All elements are uniformly distributed, indicating that the composition of the samples is homogeneous. On the other hand, there are areas of Sn-richness. This is considered to be Ti_6Sn_5 and Sn, as confirmed by XRD measurements.

Table 2
Elemental composition of $TiNi_{0.95-x}Co_{0.05}Sn$ ($0 \leq x \leq 0.1$, $y = 0.05$) at room temperature.

Sample composition	Nominal composition (at%)				Chemical composition (at%)				Actual Sample composition
	Ti	Ni	Co	Sn	Ti	Ni	Co	Sn	
TiNiSn	33.3	33.3	–	33.3	33.6 (1)	34.5 (1)	–	31.9 (2)	$Ti_{1.01}Ni_{1.03}Sn_{0.96}$
$TiNi_{0.95}Co_{0.05}Sn$	33.3	31.7	1.67	33.3	33.5 (4)	32.9 (1)	1.59 (1)	32.0 (4)	$Ti_{1.00}Ni_{0.99}Co_{0.05}Sn_{0.96}$
$TiNi_{0.94}Co_{0.05}Sn$	33.4	31.4	1.67	33.4	34.0 (2)	31.6 (1)	1.63 (1)	32.7 (3)	$Ti_{1.02}Ni_{0.94}Co_{0.05}Sn_{0.98}$
$TiNi_{0.92}Co_{0.05}Sn$	33.7	31.0	1.68	33.7	34.2 (1)	31.9 (3)	1.57 (1)	32.3 (3)	$Ti_{1.02}Ni_{0.95}Co_{0.05}Sn_{0.96}$
$TiNi_{0.90}Co_{0.05}Sn$	33.9	30.5	1.69	33.9	34.5 (2)	31.7 (2)	1.63 (1)	32.2 (4)	$Ti_{1.02}Ni_{0.93}Co_{0.05}Sn_{0.95}$
$TiNi_{0.87}Co_{0.05}Sn$	34.2	29.8	1.71	34.2	34.6(1)	30.7 (1)	1.54 (1)	33.2 (1)	$Ti_{1.01}Ni_{0.90}Co_{0.05}Sn_{0.97}$
$TiNi_{0.85}Co_{0.05}Sn$	34.5	29.3	1.72	34.5	35.0 (1)	30.6 (1)	1.58 (1)	32.8 (1)	$Ti_{1.02}Ni_{0.89}Co_{0.05}Sn_{0.95}$

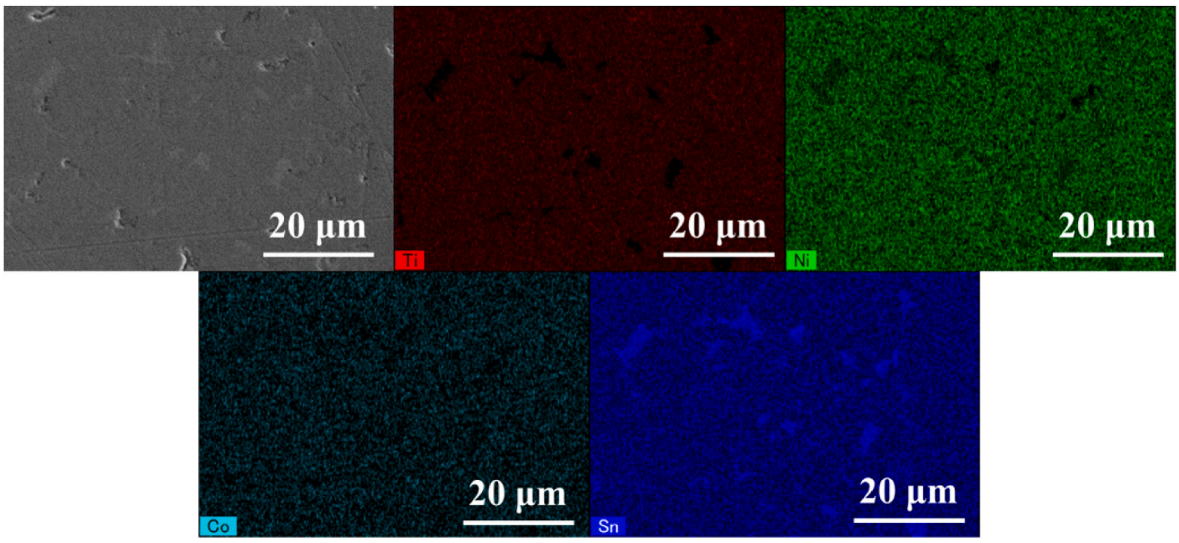

Fig. 4. SEM-EDS mapping of $TiNi_{0.95-x}Co_{0.05}Sn$ ($x = 0.1$, $y = 0.05$). Ti, Ni, Co, and Sn are mapped with red, green, cyan, and blue, respectively.

Table 3
Summary of thermoelectric properties of $TiNi_{0.95-x}Co_{0.05}Sn$ ($0 \leq x \leq 0.1$, $y = 0.05$) at room temperature, where L_0, n_H, μ_H, S, ρ, and κ are Lorenz number, Hall carrier density, Hall mobility, Seebeck coefficient, electrical resistivity, and total thermal conductivity, respectively.

Composite	x	R_H (cm^3C^{-1})	n_H (cm^{-3})	μ_H ($cm^2V^{-1}s^{-1}$)	ρ (Ωcm)	$\lvert S\rvert$ (μVK^{-1})	κ ($Wm^{-1}K^{-1}$)	L_0 ($\times 10^{-8}$ V^2K^{-2})
$TiNi_{0.95-x}Co_{0.05}Sn$	0	3.2 (1) $\times 10^{-2}$	1.9 (1) $\times 10^{20}$	1.1 (1)	2.78 $\times 10^{-2}$	192	4.73	1.658
	0.01	1.8 (1) $\times 10^{-2}$	3.5 (2) $\times 10^{20}$	0.65 (3)	2.71 $\times 10^{-2}$	175	4.66	1.676
	0.03	1.3 (1) $\times 10^{-2}$	4.9 (1) $\times 10^{20}$	2.1 (1)	6.02 $\times 10^{-3}$	180	5.59	1.670
	0.05	1.2 (1) $\times 10^{-2}$	5.4 (2) $\times 10^{20}$	1.8 (1)	6.57 $\times 10^{-3}$	173	5.80	1.679
	0.08	7.3 (3) $\times 10^{-3}$	8.6 (4) $\times 10^{20}$	1.9 (1)	3.91 $\times 10^{-3}$	141	5.78	1.747
	0.1	3.0 (2) $\times 10^{-3}$	2.1 (1) $\times 10^{21}$	0.92 (6)	3.23 $\times 10^{-3}$	62.1	5.75	2.136

3.2. Electrical transport properties

The values of Hall coefficient R_H, Hall carrier density n_H, Hall mobility μ_H, and thermoelectric properties at room temperature obtained from Hall effect measurements are summarized in Table 3 (for $y = 0.01$, 0.03 are shown Table ST3 in the SI). The carrier density n_H increases with increasing x. The mobility μ_H increases for $x = 0.03$–0.08, $y = 0.05$ from $x = 0$, $y = 0.05$. These changes are consistent with the trend for interstitial Ni atoms. Interestingly, $x = 0$–0.05, $y = 0.01$ shows N-type conduction. However, $x = 0.10$, $y = 0.01$ shows P-type conduction. This means that the decrease in Ni composition ratio resulted in the doping of hole carriers. The improvement of μ_H is attributed to the suppression of carrier scattering [30]. For $x = 0.1$, $y = 0.05$, μ_H decreases again due to an increase in the impurity phase Ti_6Sn_5. The increase in n_H is attributed to the suppression of interstitial Ni atoms, which are donor impurities. Therefore, in P-type MNiSn (M = Ti, Zr, Hf), the decrease of the Ni composition ratio is effective to improve the conduction properties.

3.3. Thermoelectric properties

Fig. 5 (a) shows the temperature dependence of electrical resistivity (ρ). Above room temperature, semiconducting behavior is observed, where the electrical resistivity decreases with increasing temperature for all samples. On the other hand, it should be noted that the ρ decreases with x due to the increase in n_H and μ_H, according to the law of $\rho = (ne\mu)^{-1}$. Fig. 5 (b) shows the temperature dependence of the Seebeck coefficient. Interestingly, up to $x = 0.05$, $y = 0.05$, the $|S|$ only slightly decreases. Usually, S has a trade-off relationship with ρ, but in our case, S does not significantly decrease for $x \leq 0.05$. To clarify the reason for this, the density of states (DOS) in the presence of interstitial Ni atoms is calculated by the ab initio calculation package AkaiKKR [42]. Fig. 5 (c) shows DOS near the Fermi level of TiNiSn. In the presence of interstitial Ni atoms, a rise of the DOS (called "in-gap states") is observed in the energy gap (E_g). In the case of stoichiometric composition, the in-gap state disappears. Therefore, the disappearance of "in-gap states" is considered to be due to the decrease in interstitial Ni atoms after the Ni composition ratio is decreased. In addition, Chen et al. reported that MNiSn (M = Ti, Zr, Hf) has a reduced band gap when interstitial Ni atoms are present, using Density Functional Theory (DFT) calculations, and it is consistent with our result. From the above, it is considered that E_g expands as x increases, and the effective mass m^* changes due to the change in the electronic structure. In fact, the m^* estimated from the relationship between n_H and $|S|$ (Pisarenko plot in Fig. 5 (d)) changes with increasing x. The m^* increases for $x > 0$, and the increase in m^* contributes to the increase in $|S|$. The relation between m^* and S can be explained by Mott's equation [43–45].

$$|S| \approx \frac{{k_B}^2}{3|e|} T \frac{m^*}{\hbar^2} \left(\frac{\pi}{3n}\right)^{\frac{2}{3}} \tag{3}$$

where $|S|$ is the absolute Seebeck coefficient, k_B is the Boltzmann constant, T is the temperature, m^* is the effective mass, $\hbar$ is the Planck constant, e is the elementary charge, and n_H is the carrier concentration. On the other hand, the decrease in $|S|$ for $x > 0.05$ is due to the increase in n_H, which is inversely related to the value of m^*, and to the increase in the impurity phase associated with the increase in x. Therefore, it is found that a decrease in the Ni composition ratio increases m^* while increasing n_H, and thus decreases ρ while maintaining the value of $|S|$. In addition, when the relaxation time is approximated as constant, $\mu_H \propto m^{*-1}$, m^* decreases due to the decrease of interstitial Ni atoms, but both μ_H and m^* increase with the increase of x. This means that the number of impurities scattering decreases due to the suppression of interstitial Ni atoms, and the relaxation time is not constant, but rather increases.

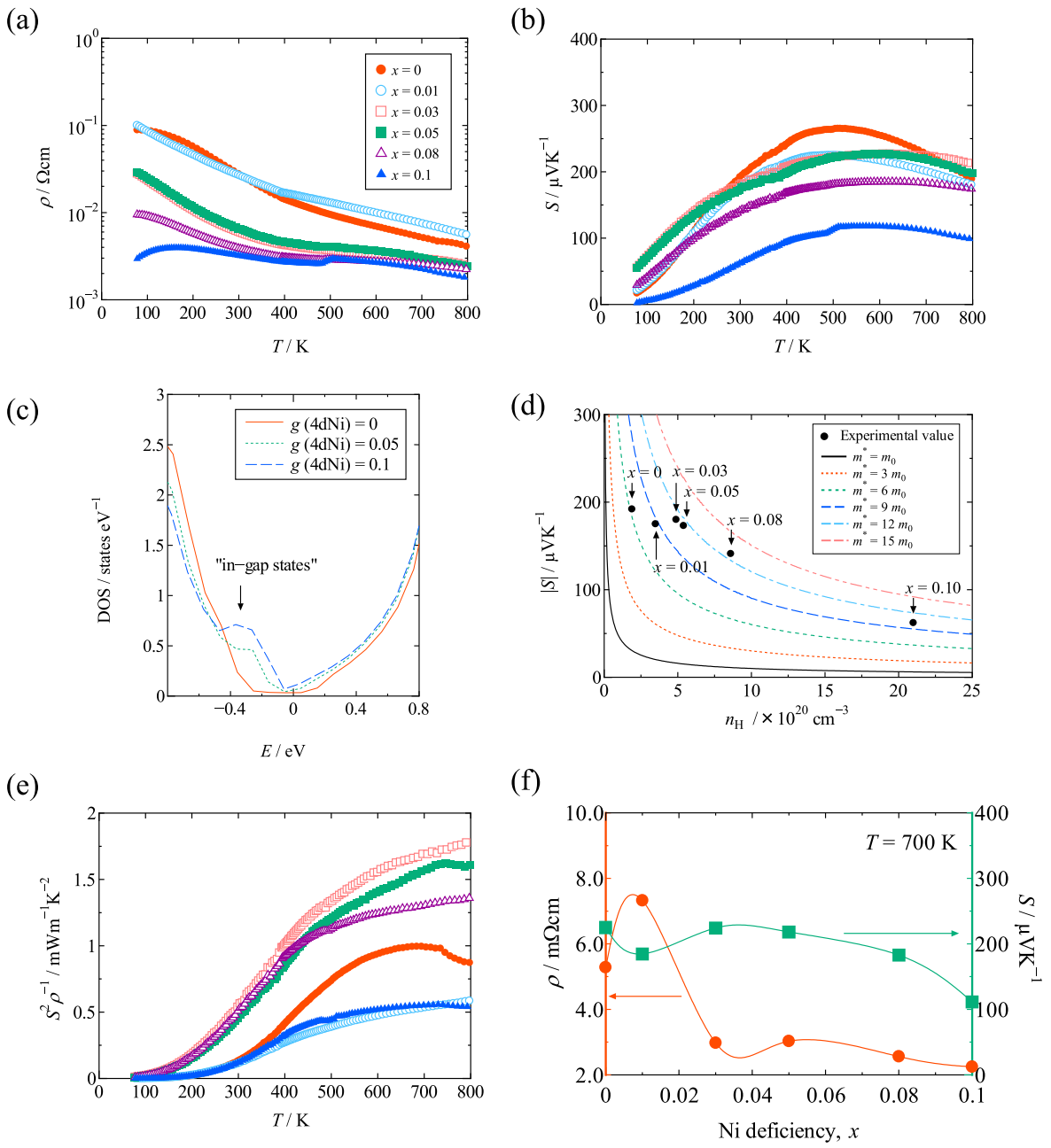

Fig. 5. (a) Temperature dependence of electrical resistivity (ρ), (b) the Seebeck coefficient (S), (c) DOS calculated by AkaiKKR for $TiNi_{1+x}Sn$ ($0 \le x \le 0.1$) near the Fermi level. (d) Absolute Seebeck coefficient $|S|$ versus carrier density (n_H) at room temperature. The solid line is the calculated data from eq. (3) using various effective masses, $m^* = x.m_e$, where x is the variables and m_e is the static mass of electrons equal to 9.10938×10^{-31} kg. (e) Power factor ($S^2\rho^{-1}$), and (f) ρ and S at 700 K for $TiNi_{0.95-x}Co_{0.05}Sn$ ($0 \le x \le 0.1$, $y = 0.05$).

Fig. 5 (e) shows the temperature dependence of the power factor (PF). The PF increases over the entire temperature range for $x = 0.03$ and $y = 0.05$. Especially at $T = 700$ K, the PF increases from 1.0 $Wm^{-1}K^{-2}$ ($x = 0$, $y = 0.05$) to 1.7 $Wm^{-1}K^{-2}$ ($x = 0.03$, $y = 0.05$). The increase in PF is attributed to the decrease in ρ and the stability of $|S|$. There are no samples in $y = 0.01$, 0.03 exceeded the Power Factor for $y = 0.05$ (Fig. S4 in the SI). Fig. 5 (f) shows the x dependence of ρ and S at $T = 700$ K. For $x > 0.01$, the ρ decreases significantly, while the value of $|S|$ remains almost unchanged up to $x = 0.05$. Therefore, the reduction of interstitial Ni atoms provides the most ideal change in charge transport properties for improving thermoelectric performance. The results also suggest that similar effects can be expected for similar compounds MNiSn (M = Ti, Zr, Hf).

Fig. 6(a) shows the temperature dependence of κ_{tot}. And Fig. 6(b) shows κ_{lat} and $\kappa_{ele} = L_0 T \rho^{-1}$ calculated from the Wiedemann-Franz law, where L_0 is the Lorenz number, and the value of the Lorenz number is determined from the experimental values of the Seebeck coefficient at room temperature using the following equation [46]. The scattering factor r is assumed to be acoustic phonon scattering, and $r = -0.5$ is used [47].

$$L_0 = \left(\frac{k_B}{e}\right)^2 \left\{ \frac{\left(r+\frac{7}{2}\right)F_{r+\frac{5}{2}}(\eta)}{\left(r+\frac{3}{2}\right)F_{r+\frac{1}{2}}(\eta)} - \left[\frac{\left(r+\frac{5}{2}\right)F_{r+\frac{3}{2}}(\eta)}{\left(r+\frac{3}{2}\right)F_{r+\frac{1}{2}}(\eta)} \right]^2 \right\} \quad (4)$$

where $F_n(\eta)$ is a function of the Fermi energy E_F with the following

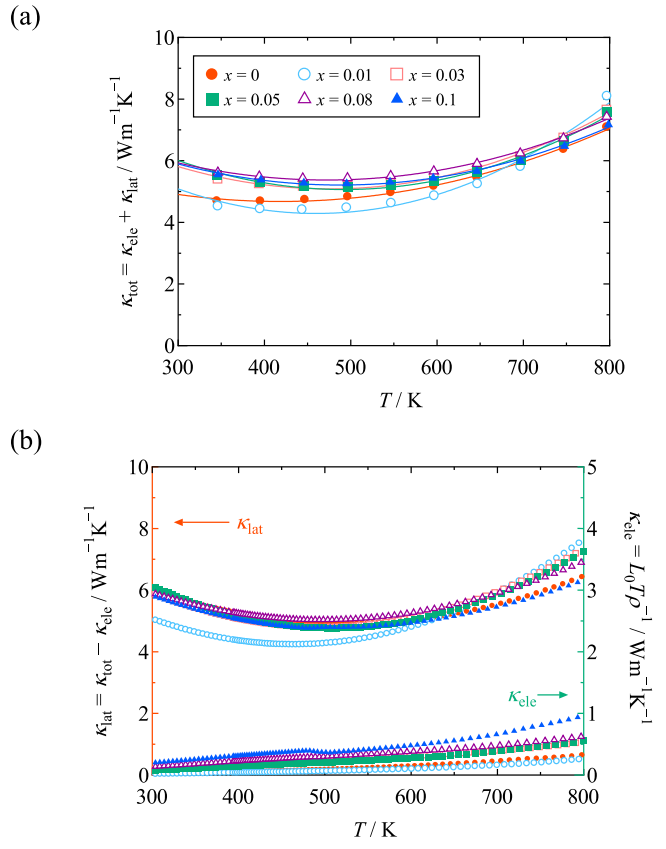

Fig. 6. Temperature dependence of (a) total thermal conductivity (κ_{tot}), (b) lattice thermal conductivity (κ_{lat}) and carrier thermal conductivity (κ_{ele}) for $TiNi_{0.95-x}Co_{0.05}Sn$ ($0 \leq x \leq 0.1$, $y = 0.05$) where $\kappa_{ele} = L_0\rho^{-1}T$ calculated by Wiedemann-Franz law.

relation

$$F_n(\eta) = \int_0^\infty \frac{\chi^n}{1 + e^{\chi-\eta}} d\chi \tag{5}$$

$$\eta = \frac{E_F}{k_B T} \tag{6}$$

Table 3 summarizes the Lorenz number for each sample. Fig. 6(a) shows that κ_{tot} slightly increases for $x > 0$. This is due to the decrease in interstitial Ni atoms, which are also phonon scattering sources. The increase at high temperature includes the effect of bipolar diffusion (κ_{bip}), which is not fully accounted for by κ_{ele}. Fig. 6(b) shows that κ_{lat} is dominant in κ_{tot}, and κ_{ele} increases with the increase of x. The increase of κ_{ele} is attributed to the decrease of ρ. Furthermore, at low temperature, despite the increase in κ_{ele}, κ_{lat} has remained almost unchanged, suggesting that κ_{lat} slightly increased. Therefore, the decrease of interstitial Ni atoms increases κ_{lat} and κ_{ele}. Thus, κ_{tot} increases over the whole temperature range. For $y = 0.01$ and 0.03, κ_{tot} also increases with an increase in x (in Fig. S5). Since the increase in κ_{tot} affects the deterioration of ZT, it is necessary to control κ_{lat} independently to further increase ZT, and heavy-element doping and fabrication methods are effective for this purpose [22,48,49].

Finally, Fig. 7(a) shows the temperature dependence of ZT (for $y = 0.01$, 0.03 are shown in Fig. S6 in the SI). For $x > 0.01$, ZT increases. In particular, for $x = 0.03$, $y = 0.05$, ZT shows a maximum value among all samples ($0 \leq x \leq 0.1$, $0.01 \leq y \leq 0.05$), $ZT_{max} = 0.18$ ($T = 700$ K). This is a 50 % improvement over $ZT_{max} = 0.12$ ($T = 675$ K) for $x = 0$, $y = 0.05$. Fig. 7(b) shows a comparison to the previous study. Although not as

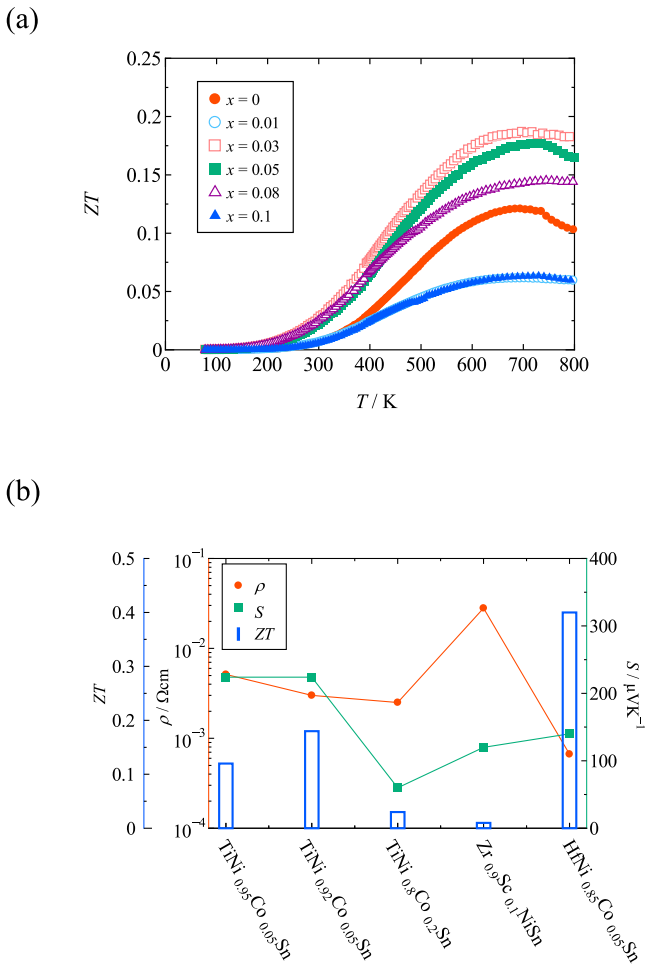

Fig. 7. (a) Temperature dependence of ZT for $TiNi_{0.95-x}Co_{0.05}Sn$ ($0 \leq x \leq 0.1$, $y = 0.05$). (b) Electrical resistivity (ρ), the Seebeck coefficient (S), and ZT ($T = 700$ K) in comparison with reported data [21,50,51].

good as expensive HfNiSn-based HH compounds, it showed a higher ZT than ZrNiSn-based compounds. The improvement in ZT is consistent with the results for the output factors, and is therefore attributable to the improvement in ρ and S. Therefore, it is clear that a reduction of κ is effective to further increase ZT. For $y = 0.03$, ZT increased for $x = 0.05$ and 0.1 compared to $x = 0$, $y = 0.03$. For $y = 0.01$, N-type conduction was observed for $x \leq 0.05$. This is due to the insufficient amount of Co doping level, resulting in a majority of carriers remaining as electrons. $x = 0.1$, $y = 0.01$ exhibited P-type conduction, but due to the low power factor and high thermal conductivity, the ZT value was the smallest among P-type materials.

Therefore, the values of x and y are closely related, and since both affect carrier density, it is necessary to achieve an optimal balance to maximize the ZT value.

4. Conclusion

In this study, to reduce the electrical resistivity by increasing the hole carrier density with the suppression of interstitial Ni atoms, $TiNi_{1-x-y}Co_ySn$ was prepared by the arc melting method, and its thermoelectric properties were investigated. The crystal structure analysis indicates that the amount of interstitial Ni atoms decreases for $x > 0.01$ and $y = 0.05$. All samples are crystallized in the HH structure, but a trace of impurity phase was formed for $x > 0.05$. The thermoelectric properties of the samples show a decrease in ρ for $x > 0.01$, which confirms

that the objective is achieved. The $|S|$ does not significantly decrease up to $x = 0.05$ and $y = 0.05$. The κ increases for $x > 0$. The ZT has a maximum over the entire temperature range for $x = 0.03$ and $y = 0.05$, and ZT_{max} is 1.5 times larger than that of the $x = 0$ and $y = 0.05$ sample. These results show that the performance can be improved by simply decreasing the Ni composition ratio without any special manipulations or raw materials, and thus contribute greatly to the provision of practical thermoelectric materials. Although the ZT obtained in this study ($ZT = 0.18$) is still limited compared to a practical value, further improvement is possible by reducing the thermal conductivity of the lattice.

CRediT authorship contribution statement

Kosuke Yamazaki: Writing – original draft, Visualization, Methodology, Investigation, Formal analysis, Data curation, Conceptualization. **Sopheap Sam:** Writing – review & editing. **Hiroshi Nakatsugawa:** Validation, Supervision, Software, Resources, Project administration, Funding acquisition.

Declaration of competing interest

The authors declare that they have no known competing financial interests or personal relationships that could have appeared to influence the work reported in this paper.

Acknowledgments

XRD, SEM, and ICP -OES were conducted using the equipment of the Instrumental Analysis Center at Yokohama National University. PEM-2 was performed at the National Defense Academy of Japan. In addition, the authors would like to express appreciation to Mr. Taegyun Kim for cooperating with sample preparation and measurement of thermoelectric properties at 80 K–395 K for this study.

Appendix A. Supplementary data

Supplementary data to this article can be found online at https://doi.org/10.1016/j.solidstatesciences.2025.108060.

Data availability

Data will be made available on request.

References

[1] R. Ovik Fitriani, B.D. Long, M.C. Barma, M. Riaz, M.F.M. Sabri, S.M. Said, R. Saidur, A review on nanostructures of high-temperature thermoelectric materials for waste heat recovery, Renew. Sustain. Energy Rev. 64 (2016) 635–659, https://doi.org/10.1016/j.rser.2016.06.035.

[2] H. Jouhara, N. Khordehgah, S. Almahmoud, B. Delpech, A. Chauhan, S.A. Tassou, Waste heat recovery technologies and applications, Therm. Sci. Eng. Prog. 6 (2018) 268–289, https://doi.org/10.1016/j.tsep.2018.04.017.

[3] H. Kawamoto, R&D Trends in High Efficiency Thermoelectric Conversion Materials for Waste Heat Recovery, 2009.

[4] D.M. Rowe, G. Min, Evaluation of thermoelectric modules for power generation, J. Power Sources 73 (1998) 193–198, https://doi.org/10.1016/S0378-7753(97)02801-2.

[5] M. Gao, D.M. Rowe, Optimisation of thermoelectric module geometry for 'waste heat' electric power generation, J. Power Sources 38 (1992) 253–259, https://doi.org/10.1016/0378-7753(92)80114-Q.

[6] J.R. Sootsman, D.Y. Chung, M.G. Kanatzidis, New and old concepts in thermoelectric materials, Angew Chem. Int. Ed. Engl. 48 (2009) 8616–8639, https://doi.org/10.1002/anie.200900598.

[7] J. Wei, L. Yang, Z. Ma, P. Song, M. Zhang, J. Ma, F. Yang, X. Wang, Review of current high-ZT thermoelectric materials, J. Mater. Sci. 55 (2020) 12642–12704, https://doi.org/10.1007/s10853-020-04949-0.

[8] I. Terasaki, Y. Sasago, K. Uchinokura, Large thermoelectric power inNaCo2O4single crystals, Phys. Rev. B Condens. Matter 56 (1997) R12685–R12687, https://doi.org/10.1103/physrevb.56.r12685.

[9] G. Ren, J. Lan, C. Zeng, Y. Liu, B. Zhan, S. Butt, Y.H. Lin, C.W. Nan, High performance oxides-based thermoelectric materials, J. Occup. Med. 67 (2015) 211–221, https://doi.org/10.1007/s11837-014-1218-2.

[10] A. Nozariasbmarz, A. Agarwal, Z.A. Coutant, M.J. Hall, J. Liu, R. Liu, A. Malhotra, P. Norouzzadeh, M.C. Öztürk, V.P. Ramesh, Y. Sargolzaeiaval, F. Suarez, D. Vashaee, Thermoelectric silicides: a review, Jpn. J. Appl. Phys. 56 (2017) 05DA04, https://doi.org/10.7567/JJAP.56.05DA04.

[11] A.T. Burkov, Silicide thermoelectrics: materials for energy harvesting, Physica Status Solidi (A) Applications and Materials Science 215 (2018), https://doi.org/10.1002/pssa.201800105.

[12] T. Zhu, C. Fu, H. Xie, Y. Liu, X. Zhao, High efficiency half-heusler thermoelectric materials for energy harvesting, Adv. Energy Mater. 5 (2015), https://doi.org/10.1002/aenm.201500588.

[13] J. Yu, Y. Xing, C. Hu, Z. Huang, Q. Qiu, C. Wang, K. Xia, Z. Wang, S. Bai, X. Zhao, L. Chen, T. Zhu, Half-Heusler thermoelectric module with high conversion efficiency and high power density, Adv. Energy Mater. 10 (2020), https://doi.org/10.1002/aenm.202000888.

[14] L. Huang, Q. Zhang, B. Yuan, X. Lai, X. Yan, Z. Ren, Recent progress in half-Heusler thermoelectric materials, Mater. Res. Bull. 76 (2016) 107–112, https://doi.org/10.1016/j.materresbull.2015.11.032.

[15] X. Ai, B. Lei, M.O. Cichocka, L. Giebeler, R.B. Villoro, S. Zhang, C. Scheu, N. Pérez, Q. Zhang, A. Sotnikov, D.J. Singh, K. Nielsch, R. He, Enhancing the thermoelectric properties via modulation of defects in *P*-type MNiSn-based (M = Hf, Zr, Ti) Half-Heusler materials, Adv. Funct. Mater. 33 (2023) 2305582, https://doi.org/10.1002/adfm.202305582.

[16] C. Fu, T. Zhu, Y. Liu, H. Xie, X. Zhao, Band engineering of high performance p-type FeNbSb based half-Heusler thermoelectric materials for figure of merit zT > 1, Energy Environ. Sci. 8 (2015) 216–220, https://doi.org/10.1039/c4ee03042g.

[17] G. Rogl, A. Grytsiv, M. Gürth, A. Tavassoli, C. Ebner, A. Wünschek, S. Puchegger, V. Soprunyuk, W. Schranz, E. Bauer, H. Müller, M. Zehetbauer, P. Rogl, Mechanical properties of half-Heusler alloys, Acta Mater. 107 (2016) 178–195, https://doi.org/10.1016/j.actamat.2016.01.031.

[18] K. Kurosaki, Y. Ohishi, H. Muta, S. Yamanaka, Half-Heusler compounds as promising high-performance thermoelectric materials, Netsu Sokutei 43 (2016), 2016–2016, https://www.netsu.org/JSCTANetsuSokutei/pdfs/43/43-3-91.pdf.

[19] S. Bhattacharya, A.L. Pope, R.T. Littleton IV, T.M. Tritt, V. Ponnambalam, Y. Xia, S. J. Poon, Effect of Sb doping on the thermoelectric properties of Ti-based half-Heusler compounds, $TiNiSn_{1-x}Sb_x$, Appl. Phys. Lett. 77 (2000) 2476–2478, https://doi.org/10.1063/1.1318237.

[20] C.S. Birkel, W.G. Zeier, J.E. Douglas, B.R. Lettiere, C.E. Mills, G. Seward, A. Birkel, M.L. Snedaker, Y. Zhang, G.J. Snyder, T.M. Pollock, R. Seshadri, G.D. Stucky, Rapid microwave preparation of thermoelectric TiNiSn and TiCoSb half-heusler compounds, Chem. Mater. 24 (2012) 2558–2565, https://doi.org/10.1021/cm3011343.

[21] M. Mikami, H. Miyazaki, Y. Nishino, Enhanced thermoelectric performance by Hf substitution in p-type half-Heusler TiNi0.8Co0.2Sn, Appl. Phys. Lett. 126 (2025) 133903, https://doi.org/10.1063/5.0257112.

[22] J.-L. Chen, H. Yang, C. Liu, J. Liang, L. Miao, Z. Zhang, P. Liu, K. Yoshida, C. Chen, Q. Zhang, Q. Zhou, Y. Liao, P. Wang, Z. Li, B. Peng, Strategy of extra Zr doping on the enhancement of thermoelectric performance for TiZrxNiSn synthesized by a modified solid-state reaction, ACS Appl. Mater. Interfaces 13 (2021) 48801–48809, https://doi.org/10.1021/acsami.1c14723.

[23] M. Zou, J.-F. Li, B. Du, D. Liu, T. Kita, Fabrication and thermoelectric properties of fine-grained TiNiSn compounds, J. Solid State Chem. 182 (2009) 3138–3142, https://doi.org/10.1016/j.jssc.2009.09.003.

[24] V.A. Romaka, Y.V. Stadnyk, D. Fruchart, T.I. Dominuk, L.P. Romaka, P. Rogl, A. M. Goryn, The mechanism of generation of the donor- and acceptor-type defects in the n-TiNiSn semiconductor heavily doped with Co impurity, Semiconductors 43 (2009) 1124–1130, https://doi.org/10.1134/S1063782609090036.

[25] L.L. Wang, L. Miao, Z.Y. Wang, W. Wei, R. Xiong, H.J. Liu, J. Shi, X.F. Tang, Thermoelectric performance of half-Heusler compounds TiNiSn and TiCoSb, J. Appl. Phys. 105 (2009) 013709, https://doi.org/10.1063/1.3056384.

[26] K. Yamazaki, S. Sam, Y. Okamoto, H. Nakatsugawa, Tuning conduction properties and clarifying thermoelectric performance of P-type half-Heusler alloys TiNi1-xCoxSn (0 ≤x≤ 0.15), Solid State Sci. 157 (2024) 107708, https://doi.org/10.1016/j.solidstatesciences.2024.107708.

[27] K. Chen, C. Nuttall, E. Stefanaki, K. Placha, R. Tuley, K. Simpson, J.W.G. Bos, M. J. Reece, Fast synthesis of n-type half-heusler TiNiSn thermoelectric material, Scr. Mater. 191 (2021) 71–75, https://doi.org/10.1016/j.scriptamat.2020.09.010.

[28] S.-W. Kim, Y. Kimura, Y. Mishima, High temperature thermoelectric properties of TiNiSn-based half-Heusler compounds, Intermetallics 15 (2007) 349, https://doi.org/10.1016/j.intermet.2006.08.008.

[29] V.A. Romaka, P. Rogl, V.V. Romaka, E.K. Hlil, Y.V. Stadnyk, S.M. Budgerak, Features of a priori heavy doping of the n-TiNiSn intermetallic semiconductor, Semiconductors 45 (2011) 850–856, https://doi.org/10.1134/S1063782611070190.

[30] W. Ren, H. Zhu, J. Mao, L. You, S. Song, T. Tong, J. Bao, J. Luo, Z. Wang, Z. Ren, Manipulation of Ni interstitials for realizing large power factor in TiNiSn-based materials, Adv. Electron. Mater. 5 (2019) 1900166, https://doi.org/10.1002/aelm.201900166.

[31] S.A. Barczak, J. Buckman, R.I. Smith, A.R. Baker, E. Don, I. Forbes, J.-W.G. Bos, Impact of interstitial Ni on the thermoelectric properties of the half-heusler TiNiSn, Materials 11 (2018), https://doi.org/10.3390/ma11040536.

[32] H. Hazama, M. Matsubara, R. Asahi, T. Takeuchi, Improvement of thermoelectric properties for half-Heusler TiNiSn by interstitial Ni defects, J. Appl. Phys. 110 (2011) 063710, https://doi.org/10.1063/1.3633518.

[33] A. Berche, P. Jund, Fully ab-initio determination of the thermoelectric properties of half-heusler NiTiSn: Crucial role of interstitial Ni defects, Materials 11 (2018) 868, https://doi.org/10.3390/ma11060868.

[34] L. Hu, S. Han, T. Zhu, T. Deng, C. Fu, P-type dopability in Half-Heusler thermoelectric semiconductors, npj Comput. Mater. 11 (2025) 1–10, https://doi.org/10.1038/s41524-025-01595-5.
[35] Q. Chen, L. Ma, J. Yang, L. Xi, The A-Ni chemical bond in AIIINiSb (AIII=Sc, Y, Er) half-Heusler materials triggers the formation of anomalous vacancy defects, Mater. Today Phys. 46 (2024) 101531, https://doi.org/10.1016/j.mtphys.2024.101531.
[36] Y. Sun, W. Qiu, L. Zhao, H. He, L. Yang, L. Chen, H. Deng, X. Shi, J. Tang, Defects engineering driven high power factor of ZrNiSn-based Half-Heusler thermoelectric materials, Chem. Phys. Lett. 755 (2020) 137770, https://doi.org/10.1016/j.cplett.2020.137770.
[37] H.B. Callen, The application of onsager's reciprocal relations to thermoelectric, thermomagnetic, and galvanomagnetic effects, Phys. Rev. 73 (1948) 1349–1358, https://doi.org/10.1103/PhysRev.73.1349.
[38] F. Izumi, K. Momma, Solid State Phenom. 130 (2007) 15–20.
[39] M. Gürth, A. Grytsiv, J. Vrestal, V.V. Romaka, G. Giester, E. Bauer, P. Rogl, On the constitution and thermodynamic modelling of the system Ti–Ni–Sn, RSC Adv. 5 (2015) 92270–92291, https://doi.org/10.1039/C5RA16074J.
[40] F. Aversano, A. Ferrario, S. Boldrini, C. Fanciulli, M. Baricco, A. Castellero, Thermoelectric properties of TiNiSn half heusler alloy obtained by rapid solidification and sintering, J. Mater. Eng. Perform. 27 (2018) 6306–6313, https://doi.org/10.1007/s11665-018-3735-6.
[41] J.S. Young, R.G. Reddy, Processing and thermoelectric properties of TiNiSn materials: a review, J. Mater. Eng. Perform. 28 (2019) 5917–5930, https://doi.org/10.1007/s11665-019-04386-4.
[42] H. Akai, Electronic structure Ni–Pd alloys calculated by the self-consistent KKR-CPA method, J. Phys. Soc. Jpn. 51 (1982) 468–474, https://doi.org/10.1143/JPSJ.51.468.
[43] N.F. Mott, H. Jones, The Theory of the Properties of Metals and Alloys, Clarendon Press, Oxford, 1936.
[44] J.M. Ziman, Electrons and Phonons, Oxford University press, England, 1960.
[45] N.W. Ashcroft, N.D. Mermin, Solid State Physics, Saunders Colledge Publishers, Philadelphia, 1976.
[46] L.D. Zhao, S.H. Lo, J. He, H. Li, K. Biswas, J. Androulakis, C.I. Wu, T.P. Hogan, D. Y. Chung, V.P. Dravid, M.G. Kanatzidis, High performance thermoelectrics from earth-abundant materials: enhanced figure of merit in PbS by second phase nanostructures, J. Am. Chem. Soc. 133 (2011) 20476–20487, https://doi.org/10.1021/ja208658w.
[47] L.D. Zhao, B.P. Zhang, W.S. Liu, J.F. Li, Effect of mixed grain sizes on thermoelectric performance of Bi2Te3 compound, J. Appl. Phys. 105 (2009) 023704, https://doi.org/10.1063/1.3063694.
[48] S.-J. Joo, J.-H. Son, H.S. Lee, J. Jang, B.-S. Kim, B.-K. Min, Synthesis and thermoelectric properties of ZrxTi1−xNiSn0.98Sb0.02 n-type half-Heusler materials, J. Electron. Mater. 50 (2021) 4178–4185, https://doi.org/10.1007/s11664-021-08938-0.
[49] E. Rausch, B. Balke, T. Deschauer, S. Ouardi, C. Felser, Charge carrier concentration optimization of thermoelectric p-type half-Heusler compounds, APL Mater. 3 (2015) 041516, https://doi.org/10.1063/1.4916526.
[50] J. Schmitt, Z.M. Gibbs, G. Jeffrey Snyder, C. Felser, Resolving the true band gap of ZrNiSn half-Heusler thermoelectric materials, Mater. Horiz. 2 (2014) 68–75, https://doi.org/10.1039/C4MH00142G.
[51] X. Ai, W. Xue, L. Giebeler, N. Pérez, B. Lei, Y. Zhang, Q. Zhang, K. Nielsch, Y. Wang, R. He, Interstitial defect modulation promotes thermoelectric properties of *p*-type HfNiSn, Adv. Energy Mater. (2024) 2401345, https://doi.org/10.1002/aenm.202401345.